Chemosphere 301 (2022) 134766

Contents lists available at ScienceDirect

Chemosphere

journal homepage: www.elsevier.com/locate/chemosphere

Carbendazim imprinted electrochemical sensor based on $CdMoO_4$/g-C_3N_4 nanocomposite: Application to fruit juice samples

Mehmet Lütfi Yola

Hasan Kalyoncu University, Faculty of Health Sciences, Department of Nutrition and Dietetics, Gaziantep, Turkey

HIGHLIGHTS

- Molecularly imprinting electrochemical sensor is developed for carbendazim as fungicide detection.
- The some features of prepared electrochemical sensor are investigated.
- The superior performance of electrochemical sensor is presented.
- This sensor has some advantages such as sensitivity and selectivity.

GRAPHICAL ABSTRACT

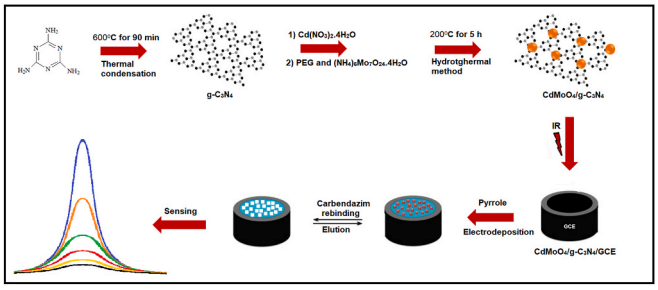

ARTICLE INFO

Handling editor: Yasser Vasseghian

Keywords:
Carbendazim
Electrochemical imprinting
Electrochemistry
Nanocomposite
Food safety

ABSTRACT

Carbendazim (CAR) as a fungicide is utilized for fruits and vegetables to provide diseases' control and the degradation of carbendazim having benzimidazole ring is slow. Herein, a molecularly imprinted electrochemical sensor based on $CdMoO_4$/g-C_3N_4 nanocomposite was prepared for CAR determination in fruit juice samples. Firstly, $CdMoO_4$/g-C_3N_4 nanocomposite with high yield was fabricated via one-pot *in-situ* hydrothermal approach including environmentally friendly method. Formation of CAR imprinted polymers was performed on $CdMoO_4$/g-C_3N_4 nanocomposite modified glassy carbon electrode (GCE) in presence of CAR as template and pyrrole (Py) as a monomer by cyclic voltammetry (CV) technique. Following the morphological, structural, and optical characterization of as-synthesized nanocomposite, the electrochemical techniques were also implemented to evaluate the electrochemical features of fabricated electrodes. The limit of quantification (LOQ) and limit of detection (LOD) values were calculated as 0.1×10^{-10} M, and 2.5×10^{-12} M, respectively in addition to satisfactory selectivity, stability, reproducibility and reusability. The findings revealed that the proposed CAR imprinted electrochemical sensor can be successfully employed in food safety.

1. Introduction

The toxic residues of pesticides, which are chemicals to increase food quality as well as agricultural productivity, reveal one of the most important environmental problems that need to be controlled all over the world (Yao et al., 2014; Pushparaj et al., 2022; Yavari et al., 2022). Especially in light of concerns about its harmful impacts on the individuals and environmental, it is critical to track even trace amounts of pesticide residues in food (Ozcan et al., 2021). CAR, which is one of the hazardous class-IV pesticide members, is employed to protect fruits and vegetables, nuts, grasses, and other field crops from various fungal diseases such as mold, and also to prevent problems such as rot or stain

E-mail address: mlutfi.yola@hku.edu.tr.

https://doi.org/10.1016/j.chemosphere.2022.134766
Received 8 March 2022; Received in revised form 15 April 2022; Accepted 25 April 2022
Available online 28 April 2022

formation (Bean and Henion, 1997; Subhani et al., 2013). It can be employed both in post-harvest food storage and before planting seeds by spraying or applying directly to the soil (Pourreza et al., 2015). It is resistant to degradation due to the benzimidazolic ring in its molecular structure, and it can endure in the environment for long periods, posing serious health and environmental risks (Wang et al., 2010). The utilization of CAR is restricted or banned in many countries since it can cause significant health problems such as hormonal disorders, skin problems, and even infertility when exposed to even trace amounts (Rajeswary et al., 2007; Wang et al., 2010; Dodiuk-Gad et al., 2015; Andrade et al., 2016). Thus, precise and swift monitoring of CAR levels in the water, soil, or food products is critical (Panades et al., 2000; Guo et al., 2011).

Many analytical approaches for detecting CAR have been proposed so far, most of them are chromatographic and spectroscopic methods (Pourreza et al., 2015). However, the practical application for monitoring pesticides by these techniques including high-performance liquid chromatography, mass spectroscopy, UV–Vis, capillary electrophoresis, fluorescence spectroscopy have some drawbacks such as complex pre-treatment steps and expensive instrumentation, besides not being suitable for in-situ and real-time monitoring (Reyes et al., 2003; Moral et al., 2009; Gilbert-Lopez et al., 2012; Dominguez-Alvarez et al., 2013; Jovanov et al., 2013). Miniaturization and simplicity of analytical techniques are important trends in analytical chemistry. In this regard, electrochemical sensors have gain great concern owing to their nature of easy to apply, low price, high sensitivity, swift response time, minimum chemical utilization, as well as reusability (Alavi-Tabari et al., 2018; Karaman et al., 2021c; Moghadam et al., 2021; Boyacıoğlu et al., 2022; Buledi et al., 2022; Darabi et al., 2022; Karimi-Maleh et al., 2022b, 2022c). In this context, thanks to the state-of-art development in nanotechnology, various types of nanostructures open a new avenue for modifying the electrodes to boost their electrochemical performances (Boke et al., 2020; Mohanraj et al., 2020; Karaman et al., 2021b; Karimi-Maleh et al., 2022a).

Polymeric graphitic carbon nitride (g-C_3N_4) as a remarkable heterogeneous nanomaterial has started considerable interest owing to superior advantages such as the bandgap of 2.7 eV providing tunable electronic structure and the excellent thermal stability (Wang et al., 2009b; Ong et al., 2016). Due to these chemical and physical properties, g-C_3N_4 has been utilized in some significant applications such as the determination of environmentally hazardous pollutants, sensor/biosensor development and catalysis (Cao et al., 2015; Yola et al., 2016; Fu et al., 2018). However, its useful applications have been limited owing to less charge transfer capacity into electrode surface and the recombination of photo-induced excitons. Thus, g-C_3N_4 's modification with other semiconductors and the dopping treatment with metal atoms can provide the increase of catalytic activity of g-C_3N_4 (Ong et al., 2015; Ran et al., 2015; Xue et al., 2015; Karaman et al., 2021a).

Cadmium molybdate ($CdMoO_4$) has gained important attention because of its superior physicochemical and electronic benefits providing the potential applications such as catalysis and energy recovery (Zhen et al., 2008; Liu et al., 2018). Its wide bandgap of 3–4 eV can provide active material under UV light, resulting in the increase of the absorbance capacity (Zhang et al., 2016; Huang et al., 2018). Z-scheme heterojunction development between $CdMoO_4$ and g-C_3N_4 causes the recombination of photo-induced excitons increasing catalytic performance and absorption capacity. The valance and conduction band potentials of $CdMoO_4$ are lower than those of g-C_3N_4, indicating the well-matched Z-scheme heterostructure. In literature, $CdMoO_4$/g-C_3N_4 nanocomposite was fabricated by using a thermal treatment including precipitation and be utilizied as photocatalyst for dye degradation (Chai et al., 2020), and it was prepared by a facile fabrication way for CO_2 reduction (Zhao et al., 2015).

A molecularly imprinting electrochemical carbendazim sensor based on $CdMoO_4$/g-C_3N_4 nanocomposite was presented. $CdMoO_4$ microspheres on g-C_3N_4 sheets with high efficiency were prepared by one-pot *in-situ* hydrothermal technique. Then, the molecular imprinting technique was performed on $CdMoO_4$/g-C_3N_4 nanocomposite surface. The functional monomers initially form a complex with the target molecule, and after the polymerization treatment, the surface functionalities of these molecules are held in the desired position. Thus, desorption of the target molecule can provide binding sites which are complementary to the analyte (Beytur et al., 2018; Ozkan et al., 2019; Karimi-Maleh et al., 2021). As a result, the manufactured molecularly imprinted electrochemical sensor provided exceptional selectivity with no interference, high sensitivity with LOD of 2.5×10^{-12} M, ease of use, and health and environmental compatibility. As a consequence, this research lays the framework for the engineering of an extremely selective and sensitive imprinted electrochemical sensor for monitoring the level of carbendazim to provide food safety.

2. Materials and methods

2.1. Chemicals and apparatus

Carbendazim (CAR, 97.0%), diquat dibromide monohydrate (DDM, 98.0%), sodium sulfate (SOS, ≥99.0%), sodium nitrate (SON, ≥99.0%), tebuconazole (TEB, ≥99.0%), pyraclostrobin (PYR), melamine, cadmium nitrate tetrahydrate ($Cd(NO_3)_2{\cdot}4H_2O$, ≥99.0%), polyethyleneglycol (PEG, ≥99.0%), ammonium molybdate tetrahydrate ($(NH_4)_6Mo_7O_{24}{\cdot}4H_2O$, ≥99.0%) and monomer (Py, ≥99.0%) were maintained by Sigma-Aldrich for nanocomposite preparation, sensor development and sensor performance measurement. A pH neutral phosphate-buffered saline (PBS) (1.0×10^{-1} M) was chosen to be employed as a supporting electrolyte, besides a dilution buffer solution.

SEM, HRTEM, XRD, and XPS analysis techniques were implemented to examine the physicochemical features of the nanostructures. On the other hand, to get further insight to the electrochemical behaviors of the constructed electrodes CV, electrochemical empedance spectroscopy (EIS), and differential pulse voltammetry (DPV) analysis were implemented by Gamry Reference 600 potensiostat-galvanostat (See Supplementary Data file for detailed information about the equipments).

2.2. Production pathway of g-C_3N_4 and $CdMoO_4$/g-C_3N_4 nanocomposite

A thermal condensation technique was used for the preparation of g-C_3N_4 in the presence of melamine as a precursor. Briefly, melamine (10.0 g) was placed in an alumina boat and the thermal annealing was performed at 600 °C over 90 min with a heating rate of 10.0 °C min^{-1}. Consequently, the yellow product (***g-C_3N_4***) was powdered and collected for subsequent usage.

The *in-situ* hydrothermal approach was conducted for the production of $CdMoO_4$/g-C_3N_4 nanocomposites. Firstly, g-C_3N_4 (30.0 g) was dissolved in ultra-pure distilled water (30.0 mL). Subsequently, $Cd(NO_3)_2{\cdot}4H_2O$ (2.0 mmol) was introduced into g-C_3N_4 solution under vigorious stirring during 45 min (Solution A). Following, PEG (40.0 mmol) and $(NH_4)_6Mo_7O_{24}{\cdot}4H_2O$ (2.0 mmol) were mixed together at 25 °C over the period of 45 min (Solution B). Afterward, Solution B was gently added into Solutin An under stirring for 45 min at 25 °C. The final solution was transferred to a Teflon-lined autoclave and heated to 200 °C with a heating rate of 5.0 °C min^{-1} and kept at this temperature over 5 h. After the cooling treatment to 25 °C, ***$CdMoO_4$/g-C_3N_4*** nanocomposite was washed with ethyl alcohol three times and dried at 25 °C. A series of $CdMoO_4$/g-C_3N_4 nanocomposites were synthesized with different ratios of $CdMoO_4$ to g-C_3N_4 ($CdMoO_4$/g–C_3N_4–5, $CdMoO_4$/g–C_3N_4–10 and $CdMoO_4$/g–C_3N_4–15).

2.3. Fabrication of $CdMoO_4$/g-C_3N_4 modified GCE

The glassy carbon electrode that was polished according to previously the reported procedure (Yola et al., 2012) (See Supplementary Data file for detailed information) was modified by gently dropping each of $CdMoO_4$/g-C_3N_4 dispersion (20.0 μL, 0.2 mg mL^{-1}) onto the surface

of it. Following that, it was exposed to an infrared heat lamp over 30 min to evaporate the solvent, resulting in $CdMoO_4$/g-C_3N_4 modified GCE (***$CdMoO_4$/g-C_3N_4/GCE***). Finally, the CdMoO4 modified GCE (***$CdMoO_4$/GCE)*** was constructed using the same construction process.

2.4. Fabrication protocol of CAR imprinted sensor and the studies of CAR removal from the electrode surface

The molecular imprinting of CAR on $CdMoO_4$/g-C_3N_4/GCE (***MIP/$CdMoO_4$/g-C_3N_4/GCE***) was conducted in the existence of 100.0 mM Py as a monomer in 0.1 M PBS solution with a pH value of 7.0 containing 25.0 mM CAR. This procedure was performed in the potential range of +0.30 V to +1.20 V via CV technique over the 20 consecutive CV cycle at a potential scan rate of 50 mV s^{-1}. CAR non-imprinted polymer on $CdMoO_4$/g-C_3N_4/GCE (***NIP/$CdMoO_4$/g-C_3N_4/GCE***) was also successfully prepared without CAR by same fabrication method. Lastly, MIP/bare GCE and MIP/CdMoO4/GCE were made using the same manufacturing process. Scheme 1 showed the fabrication protocol of $CdMoO_4$/g-C_3N_4 nanocomposite and CAR imprinted electrochemical electrode. To achieve desorption of CAR molecules, all CAR imprinted electrodes were first immersed in a bath containing 20.0 mL NaCl solution (1.0 M) and the shaking treatment was carried out during elution time of 20 min and CAR imprinting electrodes were dired at 25 °C.

2.5. Sample preparation

The packed bottles of commercial apple and orange juice samples were obtained from a supermarket. These fruit juice samples were prepared according to the methodology previously outlined in order to be suitable for the forthcoming experiments (Karimi-Maleh et al., 2021).

3. Results and discussion

3.1. Characterizations of $CdMoO_4$, g-C_3N_4 and $CdMoO_4$/g-C_3N_4 nanocomposite

XRD studies were carried out for the exploring of the crystalline structures of $CdMoO_4$, g-C_3N_4 and $CdMoO_4$/g-C_3N_4 nanocomposite (Fig. 1A). The whole specific XRD peaks relating to $CdMoO_4$ were observed in tetragonal phase because of XRD peaks attributing to (112), (004), (200), (211), (204), (220), (116), (312), (224), (008), (400), and (316) crystal planes which were corresponded to $2\theta = 30.08°$, 32.18°, 35.17°, 40.07°, 48.13°, 50.82°, 55.07°, 59.17°, 60.93°, 66.91°, 73.67°, and 78.09°, respectively. According to the XRD spectra of $CdMoO_4$, there were no obvious impurity peaks, suggesting the pure tetragonal phase formation (Wang et al., 2012; Gandamalla et al., 2021). For g-C_3N_4, the major XRD peak appeared at 28.03° corresponding to (002) plane demonstrated g-C_3N_4's interplanar stacking, and the minor XRD peak at 13.97° was attributed to (001) in-plane (Groenewolt and Antonietti, 2005). In $CdMoO_4$/g-C_3N_4 nanocomposite, the crystal planes belonging to $CdMoO_4$, and g-C_3N_4 confirmed the successful preparation of $CdMoO_4$/g-C_3N_4 nanocomposite. According to Fig. 1B, the intensity of major XRD peak at 28.03° corresponding to g-C_3N_4 reduced by increasing the concentration of $CdMoO_4$. The intensity of XRD peak at 30.08° attributing to $CdMoO_4$ increased with the increase of $CdMoO_4$ concentration. Hence, it was concluded that the co-existence of $CdMoO_4$ and g-C_3N_4 in nanocomposite was verified. Finally, the whole XRD peaks attributing to $CdMoO_4$ was shifted to higher XRD angles, showing the successful heterojunction between $CdMoO_4$ and g-C_3N_4.

FTIR spectra (Fig. S1A) were provided for the investigation of the structural vibrations and functional groups belonging to g-C_3N_4, $CdMoO_4$, and $CdMoO_4$/g-C_3N_4 nanocomposite. For g-C_3N_4, the specific absorption band at 810 cm^{-1} was attributed to s-triazine ring stretching, the absorption bands at 1573 cm^{-1}, 1408 cm^{-1}, 1330 cm^{-1}, and 1250 cm^{-1} corresponded to the aromatic C–N stretching whereas the absorption band at 1640 cm^{-1} was related to –CN stretching vibrations. The broad absorption band in range the of 3100–3350 cm^{-1} corresponded to the vibrational mode of residual $–NH_2$ functional groups (Jo et al., 2018; Manchala et al., 2019). According to the FTIR spectrum of $CdMoO_4$, the absorption bands at 440 cm^{-1} and 795 cm^{-1} were attributed to the bending and asymmetric stretching modes having Mo–O–Mo and Mo–O groups in MoO_4^{2-} tetrahedron, respectively. The absorption band at 3435 cm^{-1} corresponding to O–H stretching and the bands at 1430 cm^{-1} and 1625 cm^{-1} attributing to H–O–H vibrations were observed owing to H_2O molecules' adsorption (Lin et al., 2013; Hosseinpour-Mashkani et al., 2016). For FTIR spectra of $CdMoO_4$/g-C_3N_4 nanocomposites, the specific absorption bands for $CdMoO_4$ (795 cm^{-1}) and g-C_3N_4 (810 cm^{-1}) were overlayed, and these bands were expanded with the increase of $CdMoO_4$ concentration.

Thermogravimetric analysis (TGA) experiments (Fig. S1B) were provided for the confirmation of $CdMoO_4$ amount in the nanocomposite. For the TGA curve of g-C_3N_4, the mass loss was 100.0% owing to g-C_3N_4 burning in the temperature range of 525–760 °C. For the TGA curve of $CdMoO_4$, there was no mass loss until 810 °C. According to the TGA curves of the nanomaterials, the weight losses of $CdMoO_4$ were calculated as 5.9% for $CdMoO_4$/g–C_3N_4–5, 11.1% for $CdMoO_4$/g–C_3N_4–10, and 17.4% for $CdMoO_4$/g–C_3N_4–15 by the residual weight (Zhao et al., 2015). Hence, the successful synthesis of $CdMoO_4$/g-C_3N_4 nanocomposite was proven once again.

SEM images were obtained to explore the surface morphology and elemental composition of $CdMoO_4$, g-C_3N_4, and $CdMoO_4$/g-C_3N_4 nanostructures. According to Fig. 2A, $CdMoO_4$ with small spherical structure was observed. Fig. 2B demonstrated g-C_3N_4 having identical sheets. Fig. 2C showed SEM image of $CdMoO_4$/g–C_3N_4–15 indicating $CdMoO_4$'s spherical form (blue circles) on g-C_3N_4 surface. According to EDX graph (Fig. S2), the whole elements in $CdMoO_4$ and g-C_3N_4 were observed in $CdMoO_4$/g–C_3N_4–15 nanocomposite. Finally, HRTEM image (Fig. S3) of $CdMoO_4$/g–C_3N_4–15 confirmed the presence of $CdMoO_4$ and g-C_3N_4 in nanocomposite.

The optical properties of $CdMoO_4$, g-C_3N_4, and $CdMoO_4$/g-C_3N_4 nanostructures were assessed by UV–Vis spectroscopy (Fig. S4A). The absorption bands for g-C_3N_4, and $CdMoO_4$ were observed at 410 nm, and 310 nm, respectively. After the complex formation between g-C_3N_4 and $CdMoO_4$, the absorption bands of nanocomposites were found in between those of g-C_3N_4 and $CdMoO_4$. A little blue shift in absorption bands of nanocomposites occurred after the formation of nanocomposites, suggesting the efficient interaction of $CdMoO_4$ with g-C_3N_4. Furthermore, the absorption bands of $CdMoO_4$/g-C_3N_4 nanocomposites shifted to a higher wavelength in comparison to $CdMoO_4$. The absorption bands of nanocomposites showed a blue shift with the increase of $CdMoO_4$ amount, providing the heterojunction formation between $CdMoO_4$ and g-C_3N_4. Finally, the high absorption ability of $CdMoO_4$/g-C_3N_4 nanocomposites provided the more photogenerated charge carriers.

According to photoluminescence spectroscopy (PL) spectra (Fig. S4B), the excitation, and emission wavelengths of $CdMoO_4$ were obtained as 312 nm, and 368 nm, respectively. This situation was owing to the charge-transfer transition from O_2's ligand orbital to Mo4d metal orbital in MoO_4^{2-} complex (Liu et al., 2014). The excitation, and emission wavelengths of g-C_3N_4 were determined as 370 nm, and 472 nm, respectively. The highest emission peak intensity belonging to g-C_3N_4 suggested the recombination of photogenerated excitons (Tonda and Jo, 2018). Nonetheless, the PL intensity of nanocomposites was suppressed due to the interfacial charge transfer between $CdMoO_4$ and g-C_3N_4 via Z-scheme, providing the suppression of photogenerated excitons recombination (Zhao et al., 2015). The surface areas and pore diameters of g-C_3N_4, $CdMoO_4$, $CdMoO_4$/g–C_3N_4–15 nanocomposite were evaluated by nitrogen adsorption-desorption measurements. According to Fig. S5A and Fig. S5B, the specific surface areas, and pore volumes of g-C_3N_4, $CdMoO_4$, $CdMoO_4$/g–C_3N_4–15 nanocomposite were calculated as 18.09, 2.17, and 9.37 $m^2\ g^{-1}$, and 0.0089, 0.003, and, 0.0046 cc g^{-1}, respectively. It was concluded that g-C_3N_4 had the boosting effect on the

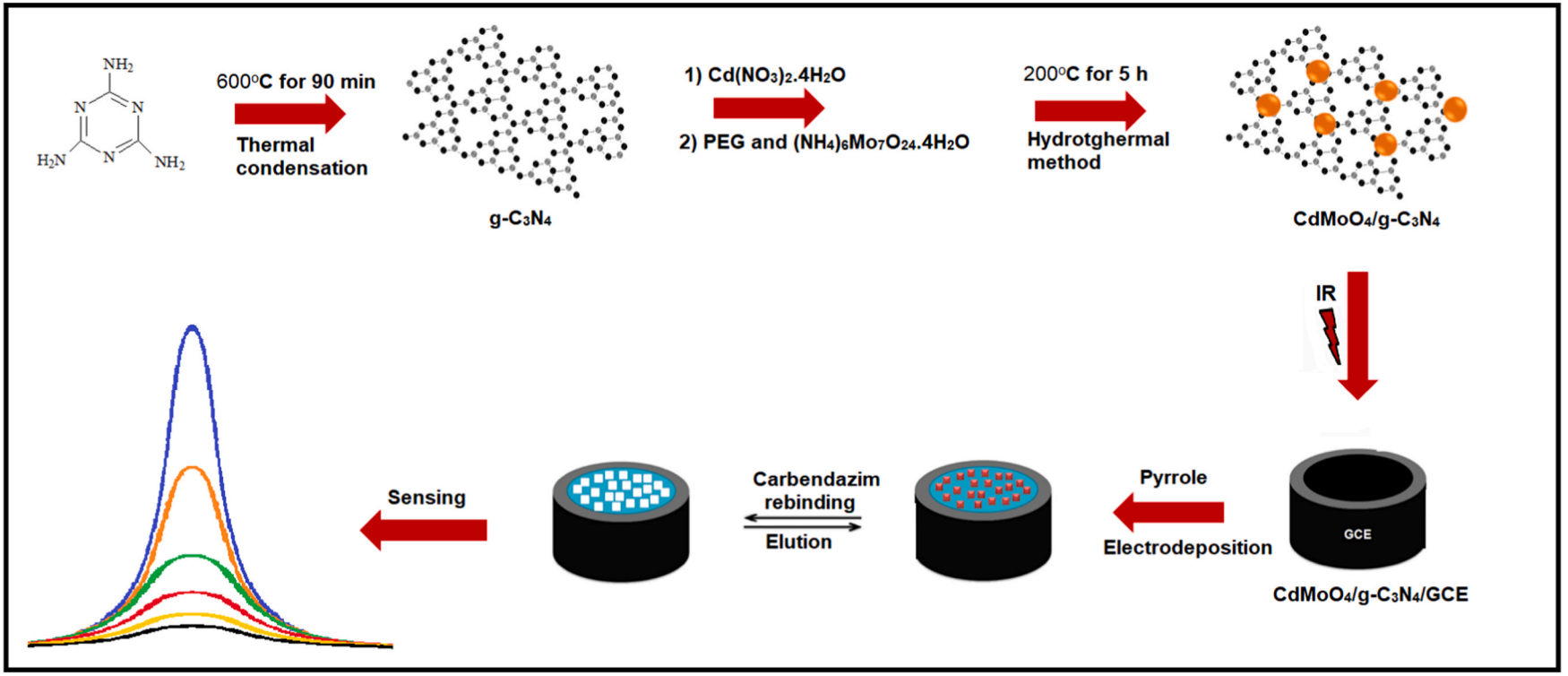

Scheme 1. Preparation protocol of $CdMoO_4$/g-C_3N_4 nanocomposite and CAR imprinted electrochemical electrode.

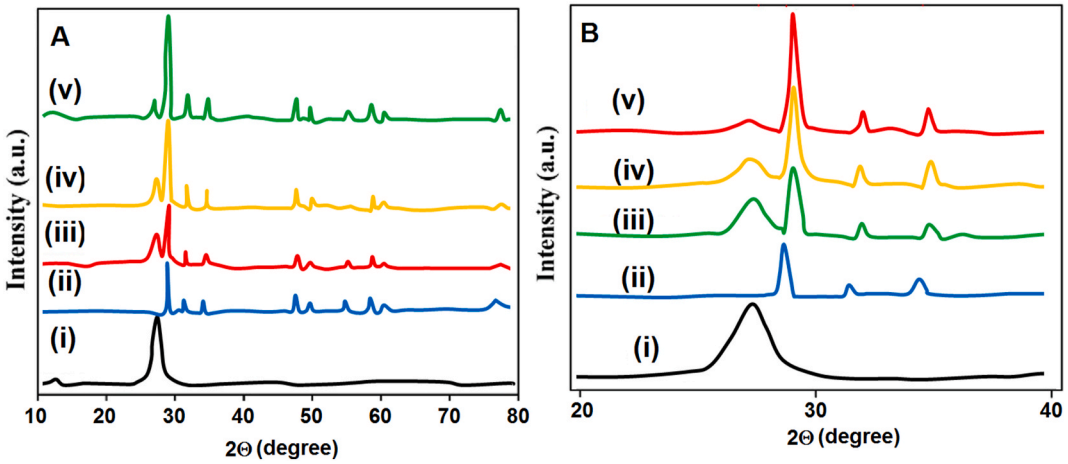

Fig. 1. (A) XRD spectra of (i) g-C_3N_4, (ii) $CdMoO_4$, (iii) $CdMoO_4$/g–C_3N_4–5, (iv) $CdMoO_4$/g–C_3N_4–10, (v) $CdMoO_4$/g–C_3N_4–15 and (B) Narrow zone XRD patterns.

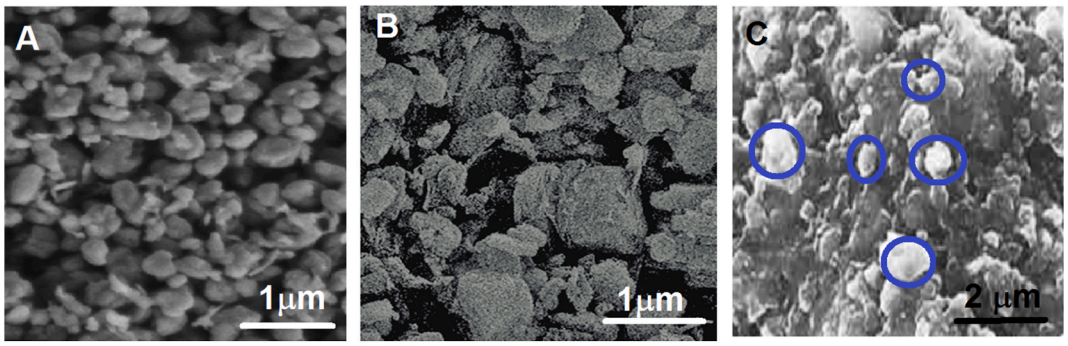

Fig. 2. SEM micrographs of (A) $CdMoO_4$, (B) g-C_3N_4 and (C) $CdMoO_4$/g–C_3N_4–15 nanostructures.

specific surface area whereas $CdMoO_4$ was of a decreasing effect on the surface area (Mezan et al., 2021). Finally, because of $CdMoO_4$'s suppression effect on charge transfer resistance, $CdMoO_4$/g–C_3N_4–15 nanocomposite was used as electrode platform for sensor applications.

The valance states and elemental composition of g-C_3N_4, $CdMoO_4$ and $CdMoO_4$/g–C_3N_4–15 nanocomposite were investigated by using XPS (Fig. S6). XPS survey (Fig. S6A) of g-C_3N_4, $CdMoO_4$ and $CdMoO_4$/g–C_3N_4–15 nanocomposite confirmed the presence of Cd, Mo, O, N and C at 405.12 eV (Cd 3d), 233.11 eV (Mo 3d), 397.19 eV (N 1s), 286.06 eV (C 1s), and 530.17 eV (O 1s), respectively, thereby providing the presence of g-C_3N_4 and $CdMoO_4$ in $CdMoO_4$/g–C_3N_4–15 nanocomposite (Zhao et al., 2015; Chai et al., 2020). According to Fig. S6B, XPS peaks observed at 285.82 eV, 289.89 eV, 290.32 eV for g-C_3N_4 and 286.29 eV, 288.56 eV, 290.68 eV for $CdMoO_4$/g–C_3N_4–15 were attributed to surface carbon, sp^2 aromatic carbon (N–C═N), and C–N–C groups, confirming the presence of g-C_3N_4 in $CdMoO_4$/g–C_3N_4–15 nanocomposite, respectively (Groenewolt and Antonietti, 2005). For N1s high-resolution XPS spectrum (Fig. S6C), 399.66 eV, 400.18 eV, 405.18 eV for g-C_3N_4 and 399.27 eV, 400.07 eV, 406.19 eV for $CdMoO_4$/g–C_3N_4–15 were corresponded to triazine rings relating to sp^2 nitrogen, tertiary nitrogen bonded to carbon (N–$(C)_3$), and amino groups (C–N–H), respectively. The two doublets with Cd^{3+} and Cd^{2+} were observed on the high-resolution Cd3d spectrum (Fig. S6D). The peaks observed at 407.81 eV, and 415.37 eV corresponded to Cd 3d3/2 of Cd^{3+} whereas the XPS peaks detected at 406.25 eV, and 412.63 eV were attributed to Cd 3d5/2 of Cd^{2+} valance ions in $CdMoO_4$. For $CdMoO_4$/g–C_3N_4–15, XPS peaks at 407.18 eV, and 413.14 eV were related to Cd 3d3/2 of Cd^{3+}, whereas XPS peaks at 405.11 eV, and 412.22 eV were ascribed to Cd 3d5/2 of Cd^{2+} in the Cd valance ions (Zeng et al., 2015). According to Fig. S6E, two specific oxidation states Mo^{6+} and Mo^{5+} were observed. XPS peaks found at 233.11 eV, and 237.21 eV were attributed to Mo 3d3/2 suggesting Mo valance ions, and the peaks detected at 232.11 eV and 236.19 eV were assigned to Mo 3d5/2, thereby confirming Mo valance ions in the Mo^{5+} of $CdMoO_4$. In addition, XPS peaks at 233.08 eV, and 237.11 eV were corresponded to Mo 3d3/2 of Mo^{6+}, and the peaks at 231.89 eV and 234.61 eV were attributed to Mo 3d5/2 of Mo^{5+} of $CdMoO_4$/g–C_3N_4–15 (Adhikari et al., 2013). For O1s high-resolution XPS spectrum (Fig. S6F), XPS peaks at 531.11 eV, 533.08 eV and 532.17 eV, and 534.27 eV were corresponded to O^{2-} ions, chemisorbed oxygen species, and C–O bonds, respectively. The binding energies of $CdMoO_4$/g–C_3N_4–15 nanocomposite were shifted to higher energy in comparison with $CdMoO_4$. Lastly, the whole XPS results confirmed the successful formation of $CdMoO_4$/g–C_3N_4–15 nanocomposite containing interfacial contact between $CdMoO_4$ and g-C_3N_4.

3.2. *Evaluation of electrochemical features of $CdMoO_4$ and $CdMoO_4$/g-C_3N_4 nanocomposites modified electrodes*

The electrochemical properties of the $CdMoO_4$ and $CdMoO_4$/g-C_3N_4 nanocomposites modified electrodes were explored via CV and EIS techniques in the existence of 1.0 mM $[Fe(CN)_6]^{3-/4-}$ redox couple. Using bare GCE, an anodic, and a cathodic peaks were initially appeared at +0.400 V, and +0.200 V, respectively (curve a of Fig. 3A). Following the implementation of $CdMoO_4$ modified GCE (curve b of Fig. 3A), the obvious enhancement in the electrochemical reply was detected owing to its physical and electronic advantages (Liu et al., 2018). When $CdMoO_4$/g-C_3N_4 nanocomposite modified electrodes (curve c-e of Fig. 3A) were applied to 1.0 mM $[Fe(CN)_6]^{3-/4-}$, the augmented electrochemical performances were attained as compared to $CdMoO_4$/GCE thanks to the higher surface area and catalysis effect of $CdMoO_4$/g-C_3N_4

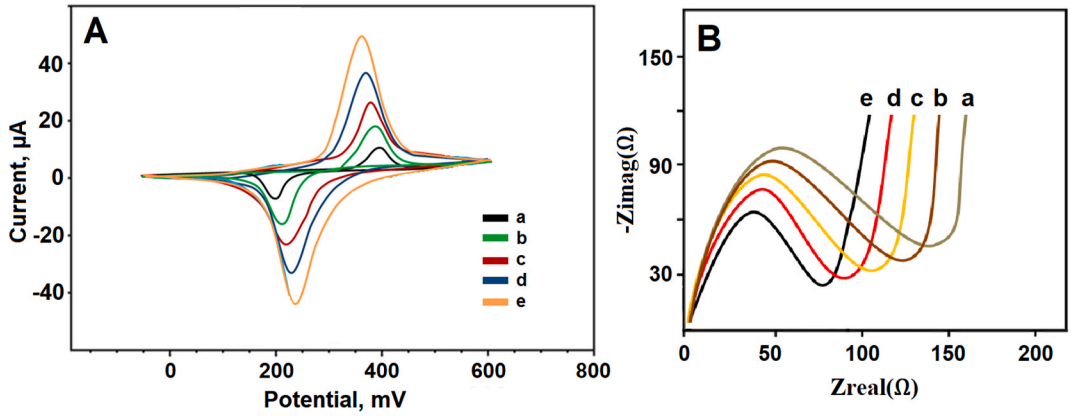

Fig. 3. (A) CV curves and (B) EIS responses at (a) bare GCE, (b) $CdMoO_4$/GCE, (c) $CdMoO_4$/g–C_3N_4–5/GCE, (d) $CdMoO_4$/g–C_3N_4–10/GCE, (e) $CdMoO_4$/g–C_3N_4–15/GCE, (Redox probe: 1.0 mM $[Fe(CN)_6]^{3-/4-}$ containing 0.1 M KCl, potential scan rate: 50 mV s^{-1}).

nanostructure (Ong et al., 2015; Yola et al., 2016). According to the collected CV curves (curve c-e of Fig. 3A), $CdMoO_4$/g–C_3N_4–15/GCE offered the greatest electrochemical performance compared to $CdMoO_4$/g–C_3N_4–10/GCE and $CdMoO_4$/g–C_3N_4–5/GCE. The values of ΔEp (anodic/cathodic potential difference) were obtained as 150 mV for $CdMoO_4$/g–C_3N_4–5/GCE, 130 mV for $CdMoO_4$/g–C_3N_4–10/GCE, and 110 mV for $CdMoO_4$/g–C_3N_4–15/GCE. Thus, when $CdMoO_4$ amount increased in nanocomposite preparation, because of Z-scheme heterojunction efficiency resulting from $CdMoO_4$, the most electro-catalytic performance was observed on $CdMoO_4$/g–C_3N_4–15/GCE (Wang et al., 2009a).

EIS measurements were used to validate the CV results (Fig. 3B). The charge transfer resistance (R_{ct}) values were reported to be 160 Ω for bare GCE (curve a), 140 Ω for $CdMoO_4$ modified GCE (curve b), 120 Ω for $CdMoO_4$/g–C_3N_4–5 modified GCE (curve c), 100 Ω for $CdMoO_4$/g–C_3N_4–10 modified GCE (curve d), and 80 Ω for $CdMoO_4$/g–C_3N_4–15 modified GCE (curve e). Because of the least charge transfer resistance, the most efficient charge transfer occurred on $CdMoO_4$/g–C_3N_4–15/GCE. The findings may point to the notion that cyclic voltammetry and electrochemical empedance spectroscopy analysis were in well-accordance.

3.3. Fabrication of CAR imprinted polymer on $CdMoO_4$/g–C_3N_4–15/GCE

Fig. S7A showed the polymerization treatment voltammograms in 25.0 mM CAR included 100.0 mM Py on $CdMoO_4$/g–C_3N_4–15/GCE. Afterward, electrooxidation current signals at 1.0 V began to gradually decrease with subsequent scans and almost disappeared in 20th cycle, indicating polymer formation on $CdMoO_4$/g–C_3N_4–15/GCE.

Differential pulse voltammograms (DPVs) were recorded by MIP/$CdMoO_4$/g–C_3N_4–15/GCE and NIP/$CdMoO_4$/g–C_3N_4–15/GCE to demonstrate the imprinting selectivity (Fig. S7B). Curve a of Fig. S7B showed no electrochemical signals without CAR molecules. The current signals on MIP/$CdMoO_4$/g–C_3N_4–15/GCE (curve c of Fig. S7B) were higher than those of NIP/$CdMoO_4$/g–C_3N_4–15/GCE (curve b of Fig. S7B) in presence of 0.5 nM CAR. Hence, the considerable selectivity was obtained by imprinting tecnique.

Lastly, distinct CAR imprinted electrochemical electrodes were prepared and applied to 0.5 nM CAR in 0.1 M PBS. According to Fig. S7C, the highest current signals were observed on MIP/$CdMoO_4$/g–C_3N_4–15/GCE in harmony with Fig. 3A and B. Anodic peak currents attributing to CAR electrooxidation also indicated an electrochemical reaction including equal electron and proton number (Fig. S8).

For morphological examination of MIP and NIP surfaces, SEM images were obtained (Fig. S9). Porous polymeric surface was obtained (Fig. S9A) and smooth polymeric surface was shown in Fig. S9B, verifing non-imprinting formation.

3.4. Optimization studies

The influences of solution pH, molar ratios of CAR to Py monomer, desorption period, and scan cycle were investigated in depth and provided in Supplementary Materials (Fig. S10).

3.5. LOQ and LOD ranges

Calibration equation of y (µA) = 9.9675x (C_{CAR}, nM) - 0.1072, (R^2 = 0.9982) by CAR amounts and DPV signals were presented in Fig. 4. LOQ, and LOD values were computed as 1.0×10^{-11} M, and 2.5×10^{-12} M, respectively (See Supplementary Data for related equations). In terms of sensitivity and linearity, Table 1 showed how the constructed electrochemical CAR sensor surpassed existing techniques. A sensitive CAR imprinted electrochemical sensor was presented in this study in the terms of LOD values and the usage of the molecularly imprinting technique provided satisfactory selectivity in fruit juice samples. Thus, an electrochemical sensor with high selectivity, and sensitivity was designed for high-efficiency CAR monitoring.

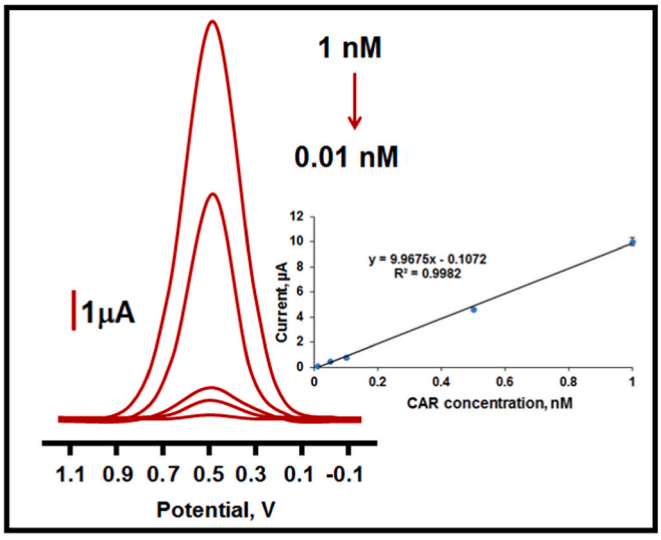

Fig. 4. DPVs with different CAR amounts at MIP/$CdMoO_4$/g–C_3N_4–15/GCE in pH 7.0 of PBS (in a concentration range of 1.0×10^{-11} - 1.0×10^{-9} M). Inset: CAR's calibration curve.

Table 1
The comparison of the as-fabricated electrochemical CAR sensor's performance metrics with various recently reported techniques.

Material	Linear Range (M)	LOD (M)	Ref.
NPG/GCE	3.0×10^{-6} – 1.2×10^{-4}	2.4×10^{-7}	Gao et al. (2019)
Glove/CSS	1.0×10^{-6} – 1.0×10^{-5}	4.7×10^{-8}	Raymundo-Pereira et al. (2021)
Cu/graphene	5.0×10^{-7} – 3.0×10^{-5}	9.0×10^{-8}	Tian et al. (2019)
SPE	1.0×10^{-7} – 1.0×10^{-6}	6.0×10^{-8}	Raymundo-Pereira et al. (2020)
PLA	1.0×10^{-7} – 1.4×10^{-6}	4.3×10^{-8}	Paschoalin et al. (2022)
CoOx/ERGO	1.0×10^{-11} – 1.0×10^{-5}	1.0×10^{-11}	Elshafey et al. (2022)
$FeSbO_4$ NPs	1.0×10^{-8} – 64.3×10^{-6}	5.4×10^{-9}	Yamuna et al. (2022)
MIP/$CdMoO_4$/g-C_3N_4-15/GCE	***1.0×10^{-11} – 1.0×10^{-9}***	***2.5×10^{-12}***	***This study***

NPG:nanoporous gold; Glove/CSS:glove-embedded carbon spherical shells; Cu/graphene: copper/graphene; SPE: screen-printed electrode; PLA: poly (lactic acid); CoOx/ERGO: cobalt oxide/electrochemically reduced graphene oxide; $FeSbO_4$ NPs: iron antimony oxide nanoparticles.

3.6. Assessment of the recovery

Two distinct fruit juice samples (Apple and Orange) were prepared for the recovery investigations. Table S1 tabulated the recovery values of CAR which were obtained by Equation (1).

$$Recovery = Found\ CAR,\ nM\ /\ Real\ CAR,\ nM \quad (1)$$

The values approaching to 100.00% (Table S1) of recovery tests validated the excellent accuracy of the as-fabricated electrochemical sensor, demonstrating the efficient detection of CAR in actual samples without any interference effect.

3.7. Evaluation of the performance of the developed electrode in terms of the selectivity, stability, reproducibility and reusability

For the selectivity assessment, five solutions that could show interference effect were prepared and the proposed electrochemical CAR sensor was applied to these five solutions. According to Fig. S11A and Fig. S11B, the obtained current signals (μA) were observed as 10.0 μA for CAR, 0.60 μA for DDM, 0.50 μA for SOS, 0.30 μA for SON, 0.20 μA for TEB, and 0.10 μA for PYR, respectively, by using MIP/$CdMoO_4$/g–C_3N_4–15/GCE and the obtained current signals (μA) were observed as 0.40 μA for CAR, 0.30 μA for DDM, 0.20 μA for SOS, 0.10 μA for SON, 0.10 μA for TEB and 0.05 μA for PYR, respectively, by using NIP/$CdMoO_4$/g–C_3N_4–15/GCE. Table S2 summarized selectivity coefficient (k) and relative selectivity coefficient (k′) values. It was found that the proposed electrochemical CAR sensor was 16.67, 20.00, 33.33, 50.00, and 100.00 times more selective for CAR against DDM, SOS, SON, TEB, and PYR, respectively, due to selective cavities of CAR molecule in polymeric structure. In addition, the obtained values on NIP/$CdMoO_4$/g–C_3N_4–15/GCE demonstrated that the molecularly imprinting technique provided satisfactory selectivity for the determination of CAR in complex samples such as fruit juice.

The collection of DPV data (Fig. S12) over a 7-week time suggested the electrochemical CAR sensor's outstanding stability. As per Fig. S12, the acquired current signal at the end of the 7-week was calculated to be ~98.61% of the obtained current signal at the end of the 1st week, showing the better stability of the as-fabricated electrochemical CAR sensor.

For the reproducibility assessment experiments, 30 individual electrochemical CAR sensors were constructed according to the previously described approach in sections 2.2-2.4. The obtained current signals had a relative standard deviation (RSD) of 0.89, indicating that the sensor fabrication technique had a high level of reliability.

Lastly, the reusability of the CAR sensor was evaluated. A high degree of reusability was verified to obtain RSD values of 0.69% having current signals during 30 times usages of the CAR sensor.

4. Conclusions

In this work, for carbendazim detection, a stable, sensitive, and selective molecularly imprinted electrochemical sensor based on $CdMoO_4$/g-C_3N_4 nanocomposite was developed. The incorporation of $CdMoO_4$ into g-C_3N_4 can enhance the electrochemical activity for carbendazim assay. This increase can be explained via two factors: (i) physical and electronic advantages of $CdMoO_4$. (ii) the enhanced electrochemical active surface area by $CdMoO_4$ improving the electron rate on electrode surface. The fabricated electrochemical sensor offered a highly sensitive detection of carbendazim with a wide linearity range (from 1.0×10^{-11} to 1.0×10^{-9} M), and a limit of detection value of 2.5×10^{-12} M, demonstrating the facile utilization of the molecularly imprinting electrochemical sensor in the food safety. The preparations of $CdMoO_4$/g-C_3N_4 nanocomposites were successfully performed by using the *in-situ* hydrothermal technique, indicating an environmentally friendly approach. The sensor demonstrated a strong affinity for carbendazim in the presence of other interfering substances. In conclusion, this work can pave the groundwork for the advancement and design of an extremely sensitive detection of pesticides in the future.

Credit author statement

Mehmet Lütfi YOLA: Supervision, Methodology, Conceptualization, Writing – review & editing.

Declaration of competing interest

The authors declare that they have no known competing financial interests or personal relationships that could have appeared to influence the work reported in this paper.

Acknowledgement

Mehmet Lütfi YOLA thanks Turkish Academy of Sciences for the supports.

Appendix A. Supplementary data

Supplementary data to this article can be found online at https://doi.org/10.1016/j.chemosphere.2022.134766.

References

Adhikari, R., Malla, S., Gyawali, G., Sekino, T., Lee, S.W., 2013. Synthesis, characterization and evaluation of the photocatalytic performance of Ag-CdMoO4 solar light driven plasmonic photocatalyst. Mater. Res. Bull. 48, 3367–3373.
Alavi-Tabari, S.A.R., Khalilzadeh, M.A., Karimi-Maleh, H., 2018. Simultaneous determination of doxorubicin and dasatinib as two breast anticancer drugs uses an amplified sensor with ionic liquid and ZnO nanoparticle. J. Electroanal. Chem. 811, 84–88.
Andrade, T.S., Henriques, J.F., Almeida, A.R., Machado, A.L., Koba, O., Giang, P.T., Soares, A.M.V.M., Domingues, I., 2016. Carbendazim exposure induces developmental, biochemical and behavioural disturbance in zebrafish embryos (vol 170, pg 390, 2016). Aquat. Toxicol. 173, 228-228.
Bean, K.A., Henion, J.D., 1997. Determination of carbendazim in soil and lake water by immunoaffinity extraction and coupled-column liquid chromatography tandem mass spectrometry. J. Chromatogr. A 791, 119–126.
Beytur, M., Kardas, F., Akyildirim, O., Ozkan, A., Bankoglu, B., Yuksek, H., Yola, M.L., Atar, N., 2018. A highly selective and sensitive voltammetric sensor with molecularly imprinted polymer based silver@gold nanoparticles/ionic liquid modified glassy carbon electrode for determination of ceftizoxime. J. Mol. Liq. 251, 212–217.
Boke, C.P., Karaman, O., Medetalibeyoglu, H., Karaman, C., Atar, N., Yola, M.L., 2020. A new approach for electrochemical detection of organochlorine compound lindane:

development of molecular imprinting polymer with polyoxometalate/carbon nitride nanotubes composite and validation. Microchem. J. 157, 105012.
Boyacıoğlu, H., Yola, B.B., Karaman, C., Karaman, O., Atar, N., Yola, M.L., 2022. A novel electrochemical kidney injury molecule-1 (KIM-1) immunosensor based covalent organic frameworks-gold nanoparticles composite and porous NiCo2S4@ CeO2 microspheres: the monitoring of acute kidney injury. Appl. Surf. Sci. 578, 152093.
Buledi, J.A., Mahar, N., Mallah, A., Solangi, A.R., Palabiyik, I.M., Qambrani, N., Karimi, F., Vasseghian, Y., Karimi-Maleh, H., 2022. Electrochemical quantification of mancozeb through tungsten oxide/reduced graphene oxide nanocomposite: a potential method for environmental remediation. Food Chem. Toxicol. 161, 112843.
Cao, S.W., Low, J.X., Yu, J.G., Jaroniec, M., 2015. Polymeric photocatalysts based on graphitic carbon nitride. Adv. Mater. 27, 2150–2176.
Chai, B., Yan, J.T., Fan, G.Z., Song, G.S., Wang, C.L., 2020. In situ fabrication of CdMoO4/g-C3N4 composites with improved charge separation and photocatalytic activity under visible light irradiation. Chin. J. Catal. 41, 170–179.
Darabi, R., Shabani-Nooshabadi, M., Karimi-Maleh, H., Gholami, A., 2022. The potential of electrochemistry for one-pot and sensitive analysis of patent blue V, tartrazine, acid violet 7 and ponceau 4R in foodstuffs using IL/Cu-BTC MOF modified sensor. Food Chem. 368, 130811.
Dodiuk-Gad, R.P., Chung, W.H., Valeyrie-Allanore, L., Shear, N.H., 2015. Stevens-johnson syndrome and toxic epidermal necrolysis: an update. Am. J. Clin. Dermatol. 16, 475–493.
Dominguez-Alvarez, J., Mateos-Vivas, M., Garcia-Gomez, D., Rodriguez-Gonzalo, E., Carabias-Martinez, R., 2013. Capillary electrophoresis coupled to mass spectrometry for the determination of anthelmintic benzimidazoles in eggs using a QuEChERS with preconcentration as sample treatment. J. Chromatogr. A 1278, 166–174.
Elshafey, R., Abo-Sobehy, G.F., Radi, A., 2022. Imprinted polypyrrole recognition film @cobalt oxide/electrochemically reduced graphene oxide nanocomposite for carbendazim sensing. J. Appl. Electrochem. 52, 45–53.
Fu, J.W., Yu, J.G., Jiang, C.J., Cheng, B., 2018. g-C3N4-Based heterostructured photocatalysts. Adv. Energy Mater. 8, 1701503.
Gandamalla, A., Manchala, S., Anand, P., Fu, Y.P., Shanker, V., 2021. Development of versatile CdMoO4/g-C3N4 nanocomposite for enhanced photoelectrochemical oxygen evolution reaction and photocatalytic dye degradation applications. Mater. Today Chem. 19, 100392.
Gao, X.Y., Gao, Y., Bian, C.C., Ma, H.Y., Liu, H.L., 2019. Electroactive nanoporous gold driven electrochemical sensor for the simultaneous detection of carbendazim and methyl parathion. Electrochim. Acta 310, 78–85.
Gilbert-Lopez, B., Garcia-Reyes, J.F., Molina-Diaz, A., 2012. Determination of fungicide residues in baby food by liquid chromatography-ion trap tandem mass spectrometry. Food Chem. 135, 780–786.
Groenewolt, M., Antonietti, M., 2005. Synthesis of g-C3N4 nanoparticles in mesoporous silica host matrices. Adv. Mater. 17, 1789.
Guo, Y.J., Guo, S.J., Li, J., Wang, E.K., Dong, S.J., 2011. Cyclodextrin-graphene hybrid nanosheets as enhanced sensing platform for ultrasensitive determination of carbendazim. Talanta 84, 60–64.
Hosseinpour-Mashkani, S.M., Maddahfar, M., Sobhani-Nasab, A., 2016. Novel silver-doped CdMoO4: synthesis, characterization, and its photocatalytic performance for methyl orange degradation through the sonochemical method. J. Mater. Sci. Mater. Electron. 27, 474–480.
Huang, J., Liu, H.H., Zhong, J.B., Yang, Q., Chen, J.F., Li, J.Z., Ma, D.M., Duan, R., 2018. Enhanced sunlight-driven photocatalytic performance of Bi-doped CdMoO4 benefited from efficient separation of photogenerated charge pairs. Solid State Sci. 80, 147–154.
Jo, W.K., Kumar, S., Eslava, S., Tonda, S., 2018. Construction of Bi2WO6/RGO/g-C3N4 2D/2D/2D hybrid Z-scheme heterojunctions with large interfacial contact area for efficient charge separation and high-performance photoreduction of CO2 and H2O into solar fuels. Appl. Catal. B Environ. 239, 586–598.
Jovanov, P., Guzsvany, V., Franko, M., Lazic, S., Sakac, M., Saric, B., Banjac, V., 2013. Multi-residue method for determination of selected neonicotinoid insecticides in honey using optimized dispersive liquid-liquid microextraction combined with liquid chromatography-tandem mass spectrometry. Talanta 111, 125–133.
Karaman, C., Karaman, O., Atar, N., Yola, M.L., 2021a. Electrochemical immunosensor development based on core-shell high-crystalline graphitic carbon nitride@carbon dots and Cd0.5Zn0.5S/d-Ti3C2Tx MXene composite for heart-type fatty acid-binding protein detection. Microchim. Acta 188, 1–15.
Karaman, C., Karaman, O., Yola, B.B., Ulker, I., Atar, N., Yola, M.L., 2021b. A novel electrochemical aflatoxin B1 immunosensor based on gold nanoparticle-decorated porous graphene nanoribbon and Ag nanocube-incorporated MoS2 nanosheets. New J. Chem. 45, 11222–11233.
Karaman, C., Yola, B.B., Karaman, O., Atar, N., Polat, I., Yola, M.L., 2021c. Sensitive sandwich-type electrochemical SARS-CoV-2 nucleocapsid protein immunosensor. Microchim. Acta 188, 1–13.
Karimi-Maleh, H., Beitollahi, H., Kumar, P.S., Tajik, S., Jahani, P.M., Karimi, F., Karaman, C., Vasseghian, Y., Baghayeri, M., Rouhi, J., Show, P.L., 2022a. Recent advances in carbon nanomaterials-based electrochemical sensors for food azo dyes detection. Food Chem. Toxicol. 164, 112961.
Karimi-Maleh, H., Karimi, F., Fu, L., Sanati, A.L., Alizadeh, M., Karaman, C., Orooji, Y., 2022b. Cyanazine herbicide monitoring as a hazardous substance by a DNA nanostructure biosensor. J. Hazard Mater. 423, 127058.
Karimi-Maleh, H., Khataee, A., Karimi, F., Baghayeri, M., Fu, L., Rouhi, J., Karaman, C., Karaman, O., Boukherroub, R., 2022c. A green and sensitive guanine-based DNA biosensor for idarubicin anticancer monitoring in biological samples: a simple and fast strategy for control of health quality in chemotherapy procedure confirmed by docking investigation. Chemosphere 291, 132928.
Karimi-Maleh, H., Yola, M.L., Atar, N., Orooji, Y., Karimi, F., Kumar, P.S., Rouhi, J., Baghayeri, M., 2021. A novel detection method for organophosphorus insecticide fenamiphos: molecularly imprinted electrochemical sensor based on core-shell Co3O4@MOF-74 nanocomposite. J. Colloid Interface Sci. 592, 174–185.
Lin, J.T., Zeng, Z., Wang, Q.M., 2013. CdMoO4:Eu3+ micro-sized luminescent particles synthesis and photo-catalytic performance. Inorg. Chim. Acta. 408, 59–63.
Liu, H.H., Huang, J., Chen, J.F., Zhong, J.B., Li, J.Z., Yang, Q., Ma, D.M., 2018. Large enhancement of sunlight-driven photocatalytic performance of CdMoO4 prepared by SDBS-assisted microwave hydrothermal method. Mater. Lett. 228, 421–423.
Liu, Y.D., Ren, L., Qi, X., Wang, Y., Liu, X.J., Zhong, J.X., 2014. One-step hydrothermal fabrication and enhancement of the photocatalytic performance of CdMoO4/CdS hybrid materials. RSC Adv. 4, 8772–8778.
Manchala, S., Tandava, V.S.R.K., Nagappagari, L.R., Venkatakrishnan, S.M., Jampaiah, D., Sabri, Y.M., Bhargava, S.K., Shanker, V., 2019. Fabrication of a novel ZnIn2S4/g-C3N4/graphene ternary nanocomposite with enhanced charge separation for efficient photocatalytic H-2 evolution under solar light illumination. Photochem. Photobiol. Sci. 18, 2952–2964.
Mezan, S.O., Al Absi, S.M., Jabbar, A.H., Roslan, M.S., Agam, M.A., 2021. Synthesis and characterization of enhanced silica nanoparticle (SiO2) prepared from rice husk ash immobilized of 3-(chloropropyl) triethoxysilanea. Mater. Today Proc. 42, 2464–2468.
Moghadam, F.H., Taher, M.A., Karimi-Maleh, H., 2021. A sensitive and fast approach for voltammetric analysis of bisphenol a as a toxic compound in food products using a Pt-SWCNTs/ionic liquid modified sensor. Food Chem. Toxicol. 152, 112166.
Mohanraj, J., Durgalakshmi, D., Rakkesh, R.A., Balakumar, S., Rajendran, S., Karimi-Maleh, H., 2020. Facile synthesis of paper based graphene electrodes for point of care devices: a double stranded DNA (dsDNA) biosensor. J. Colloid Interface Sci. 566, 463–472.
Moral, A., Sicilia, M.D., Rubio, S., 2009. Determination of benzimidazolic fungicides in fruits and vegetables by supramolecular solvent-based microextraction/liquid chromatography/fluorescence detection. Anal. Chim. Acta 650, 207–213.
Ong, W.J., Tan, L.L., Chai, S.P., Yong, S.T., Mohamed, A.R., 2015. Surface charge modification via protonation of graphitic carbon nitride (g-C3N4) for electrostatic self-assembly construction of 2D/2D reduced graphene oxide (rGO)/g-C3N4 nanostructures toward enhanced photocatalytic reduction of carbon dioxide to methane. Nano Energy 13, 757–770.
Ong, W.J., Tan, L.L., Ng, Y.H., Yong, S.T., Chai, S.P., 2016. Graphitic carbon nitride (g-C3N4)-based photocatalysts for artificial photosynthesis and environmental remediation: are we a step closer to achieving sustainability? Chem. Rev. 116, 7159–7329.
Ozcan, A., Hamid, F., Ozcan, A.A., 2021. Synthesizing of a nanocomposite based on the formation of silver nanoparticles on fumed silica to develop an electrochemical sensor for carbendazim detection. Talanta 222, 121591.
Ozkan, A., Atar, N., Yola, M.L., 2019. Enhanced surface plasmon resonance (SPR) signals based on immobilization of core-shell nanoparticles incorporated boron nitride nanosheets: development of molecularly imprinted SPR nanosensor for anticancer drug, etoposide. Biosens. Bioelectron. 130, 293–298.
Panades, P., Ibarz, A., Esplugas, S., 2000. Photodecomposition of carbendazim in aqueous solutions. Water Res. 34, 2951–2954.
Paschoalin, R.T., Gomes, N.O., Almeida, G.F., Bilatto, S., Farinas, C.S., Machado, S.A., Mattoso, L.H., Oliveira Jr., O.N., Raymundo-Pereira, P.A., 2022. Wearable sensors made with solution-blow spinning poly (lactic acid) for non-enzymatic pesticide detection in agriculture and food safety. Biosens. Bioelectron. 199, 113875.
Pourreza, N., Rastegarzadeh, S., Larki, A., 2015. Determination of fungicide carbendazim in water and soil samples using dispersive liquid-liquid microextraction and microvolume UV-vis spectrophotometry. Talanta 134, 24–29.
Pushparaj, K., Liu, W.C., Meyyazhagan, A., Orlacchio, A., Pappusamy, M., Vadivalagan, C., Robert, A.A., Arumugam, V.A., Kamyab, H., Klemes, J.J., Khademi, T., Mesbah, M., Chelliapan, S., Balasubramanian, B., 2022. Nano- from nature to nurture: a comprehensive review on facets, trends, perspectives and sustainability of nanotechnology in the food sector. Energy 240, 122732.
Rajeswary, S., Mathew, N., Akbarsha, M.A., Kalyanasundram, M., Kumaran, B., 2007. Protective effect of vitamin E against carbendazim-induced testicular toxicity-histopathological evidences and reduced residue levels in testis and serum. Arch. Toxicol. 81, 813–821.
Ran, J.R., Ma, T.Y., Gao, G.P., Du, X.W., Qiao, S.Z., 2015. Porous P-doped graphitic carbon nitride nanosheets for synergistically enhanced visible-light photocatalytic H-2 production. Energy Environ. Sci. 8, 3708–3717.
Raymundo-Pereira, P.A., Gomes, N.O., Carvalho, J.H.S., Machado, S.A.S., Oliveira, O.N., Janegitz, B.C., 2020. Simultaneous detection of quercetin and carbendazim in wine samples using disposable electrochemical sensors. Chemelectrochem 7, 3074–3081.
Raymundo-Pereira, P.A., Gomes, N.O., Shimizu, F.M., Machado, S.A.S., Oliveira, O.N., 2021. Selective and sensitive multiplexed detection of pesticides in food samples using wearable, flexible glove-embedded non-enzymatic sensors. Chem. Eng. J. 408, 127279.
Reyes, J.F.G., Barrales, P.O., Diaz, A.M., 2003. Gel-surface enhanced fluorescence sensing system coupled to a continuous-flow assembly for simultaneous monitoring of benomyl and carbendazim. Anal. Chim. Acta 493, 35–45.
Subhani, Q., Huang, Z.P., Zhu, Z.Y., Zhu, Y., 2013. Simultaneous determination of imidacloprid and carbendazim in water samples by ion chromatography with fluorescence detector and post-column photochemical reactor. Talanta 116, 127–132.
Tian, C.H., Zhang, S.F., Wang, H.B., Chen, C., Han, Z.D., Chen, M.L., Zhu, Y.Y., Cui, R.J., Zhang, G.H., 2019. Three-dimensional nanoporous copper and reduced graphene oxide composites as enhanced sensing platform for electrochemical detection of carbendazim. J. Electroanal. Chem. 847, 113243.

Tonda, S., Jo, W.K., 2018. Plasmonic Ag nanoparticles decorated NiAl-layered double hydroxide/graphitic carbon nitride nanocomposites for efficient visible-light-driven photocatalytic removal of aqueous organic pollutants. Catal. Today 315, 213–222.
Wang, W.S., Zhen, L., Xu, C.Y., Shao, W.Z., 2009a. Room temperature synthesis, growth mechanism, photocatalytic and photoluminescence properties of cadmium molybdate core-shell microspheres. Cryst. Growth Des. 9, 1558–1568.
Wang, W.S., Zhen, L., Xu, C.Y., Shao, W.Z., Chen, Z.L., 2012. Eu3+-doped CdMoO4 red phosphor synthesized through an aqueous solution route at room temperature. J. Alloys Compd. 529, 17–20.
Wang, X.C., Maeda, K., Thomas, A., Takanabe, K., Xin, G., Carlsson, J.M., Domen, K., Antonietti, M., 2009b. A metal-free polymeric photocatalyst for hydrogen production from water under visible light. Nat. Mater. 8, 76–80.
Wang, Z.C., Wang, Y.Y., Gong, F.F., Zhang, J.A., Hong, Q., Li, S.P., 2010. Biodegradation of carbendazim by a novel actinobacterium Rhodococcus jialingiae djl-6-2. Chemosphere 81, 639–644.
Xue, J.J., Ma, S.S., Zhou, Y.M., Zhang, Z.W., He, M., 2015. Facile photochemical synthesis of Au/Pt/g-C3N4 with plasmon-enhanced photocatalytic activity for antibiotic degradation. Acs Appl Mater Inter 7, 9630–9637.
Yamuna, A., Chen, T.W., Chen, S.M., 2022. Synthesis and characterizations of iron antimony oxide nanoparticles and its applications in electrochemical detection of carbendazim in apple juice and paddy water samples. Food Chem. 373, 131569.
Yao, Y.Y., Wen, Y.P., Zhang, L., Wang, Z.F., Zhang, H., Xu, J.K., 2014. Electrochemical recognition and trace-level detection of bactericide carbendazim using carboxylic group functionalized poly(3,4-ethylenedioxythiophene) mimic electrode. Anal. Chim. Acta 831, 38–49.
Yavari, S., Asadpour, R., Kamyab, H., Yavari, S., Kutty, S.R.M., Baloo, L., Abd Manan, T. S.B., Chelliapan, S., Sidik, A.B., 2022. Efficiency of carbon sorbents in mitigating polar herbicides leaching from tropical soil. Clean Technol Envir 24, 251–260.
Yola, M.L., Atar, N., Qureshi, M.S., Ustundag, Z., Solak, A.O., 2012. Electrochemically grafted etodolac film on glassy carbon for Pb(II) determination. Sensor. Actuator. B Chem. 171, 1207–1215.
Yola, M.L., Eren, T., Atar, N., 2016. A molecular imprinted voltammetric sensor based on carbon nitride nanotubes: application to determination of melamine. J. Electrochem. Soc. 163, B588–B593.
Zeng, C., Ramos-Ruiz, A., Field, J.A., Sierra-Alvarez, R., 2015. Cadmium telluride (CdTe) and cadmium selenide (CdSe) leaching behavior and surface chemistry in response to pH and O-2. J. Environ. Manag. 154, 78–85.
Zhang, H., Niu, C.G., Wen, X.J., Wang, Y., Zeng, G.M., 2016. Enhanced visible light photocatalytic activity of CdMoO4 microspheres modified with AgI nanoparticles. Catal. Commun. 86, 124–128.
Zhao, L.H., Zhang, L.H., Lin, H.J., Nong, Q.Y., Cui, M., Wu, Y., He, Y.M., 2015. Fabrication and characterization of hollow CdMoO4 coupled g-C3N4 heterojunction with enhanced photocatalytic activity. J. Hazard Mater. 299, 333–342.
Zhen, L., Wang, W.S., Xu, C.Y., Shao, W.Z., Ye, M.M., Chen, Z.L., 2008. High photocatalytic activity and photoluminescence property of hollow CdMoO4 microspheres. Scripta Mater. 58, 461–464.